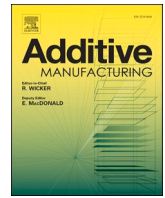# In-situ detection of stochastic spatter-driven lack of fusion: Application of optical tomography and validation via ex-situ X-ray computed tomography

(article starts on next page)

In-situ detection of stochastic spatter-driven lack of fusion: Application of optical tomography and validation via ex-situ X-ray computed tomography

Claudia Schwerz [a,*], Benjamin A. Bircher [b], Alain Küng [b], Lars Nyborg [a]

[a] *Chalmers University of Technology, Department of Industrial and Material Science, Sweden*
[b] *Federal Institute of Metrology METAS, Laboratory for Length, Nano, and Microtechnology, Switzerland*

ARTICLE INFO

ABSTRACT

The presence of random defects in laser powder bed fusion (LPBF) parts is an issue that challenges the reliability of this manufacturing process and hinders its employment in structural, defect-sensitive components. A potential solution to increase the reliability of LPBF is employing in-process monitoring targeting defect detection. This study aims to detect stochastic defects driven by spatter particles via in-situ monitoring and validate the detection method ex-situ via X-ray computed tomography (XCT). By means of in-situ optical tomography (OT), monitoring images were registered layerwise during the manufacturing of Hastelloy X specimens. The images were analyzed to detect spatters landing within specimen boundaries, and the spatial coordinates of the detections were obtained. The specimens were also measured ex-situ by means of XCT, from which key features and coordinates of internal defects were obtained. The in-situ spatter detection method was then compared to the XCT measurements. It was found that 79 % of lack of fusion defects were detected in OT images. The detection was particularly successful for large defects. Spatter-induced lack of fusion defects were present in the specimens manufactured with optimized processing parameters in different degrees, depending on the robustness of the processing conditions to spatters. This study demonstrates the applicability of optical tomography in-situ monitoring for indirect detection of stochastic lack of fusion, whose presence is inferred from spatter redeposits on the powder bed.

1. Introduction

The presence and detectability of defects in parts manufactured via laser powder bed fusion (LPBF) are pivotal to the application of this technology as a reliable industrial manufacturing method [1,2]. A class of defects particularly problematic in a real-life manufacturing scenario consists of internal, stochastic defects [3,4]. Differently from other defect classes, e.g., geometrical and surface defects [5,6], these defects are often not apparent and, due to being internal, are typically not removed by surface treatment. Additionally and more importantly, the phenomena leading to these defects are intrinsic to the manufacturing process and occur despite process parameter optimization.

A source of stochastic defects is spatter formation and redeposition in the printing area [7,8]. Spatters are byproducts of the LPBF process, whose occurrence is unpreventable [9]. The spatter particles typically present an oxidized surface [10–12] and can be much larger than the feedstock powder [8,13], thus locally disturbing the powder bed and prompting the formation of lack of fusion defects [7,14]. As a

consequence of their defect-inducing character, spatters have been associated with degradation in tensile properties [15,16] and reduced fatigue performance [17].

Considering their detrimental effect on material properties, detecting spatter-driven defects is paramount to increasing the reliability of LPBF and ensuring the components manufactured through this process present a satisfactory, predictable performance in service. However, detection of internal defects via post-manufacturing, ex-situ non-destructive inspection can be challenging and time-consuming, notably if the full design possibilities of AM are utilized and complex geometries are created [18,19]. Fortunately, in-situ monitoring can be targeted toward defect detection to improve part inspection routines [20], thereby increasing the reliability and repeatability of AM processes [2,21,22].

Concerning the in-situ detectability of spatter connected to defect formation in full-scale builds, little published data exists. Even though monitoring of spatter has been broadly explored in recent years, as compiled in a recent review article [9], only a few studies address
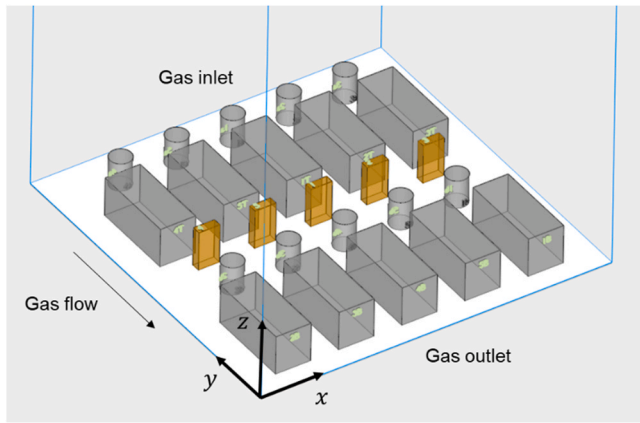

Fig. 1. Build configuration. The specimens analyzed in this study (highlighted in orange) are located halfway between the gas inlet and outlet.

spatter redeposition in the printing area, which is the factor ultimately leading to defect formation. Some studies have successfully detected spatter redeposits [23,24] and identified patterns of deposition on the powder bed [25] but have only signaled their connection to internal defects. Leung et al. [26] determined the mechanisms by which spatters create defects via micro-scale in-situ monitoring, while Coeck et al. [3] employed melt pool monitoring to detect spatter-induced defects, cross-validated with X-ray computed tomography (XCT). A limitation in these studies is the low efficiency of the monitoring data acquisition and handling, which challenges their employment in an industrial manufacturing setup. In our previous work [8,27], optical tomography (OT) was found to overcome this challenge thanks to its lean output and capability to detect redeposited spatters, which were linked to regions containing lack of fusion defects. However, a more exact correspondence between defects and in-situ detections must be established before this methodology can be used for quality control.

Hence, this study aims to determine whether individual internal defects measured via XCT can be identified through in-situ monitoring. The extent to which the in-situ detection method can match actual defects is evaluated through metrics derived from the quantification of true positive, false positive, and false negative detections. The specimens evaluated in this study were manufactured using varying but optimized sets of parameters that yield defect-free material when the effects of spatter are negligible. This variability allowed for a more general evaluation of the method proposed and led to the identification of processing

conditions more robust to spatter-induced defect formation.

2. Materials and methods

2.1. Laser powder bed fusion manufacturing

An EOS M290 (EOS GmbH Electro Optical Systems) LPBF machine was used to manufacture Hastelloy X test specimens from gas-atomized powder with particle size distribution 19 μm (d10), 35 μm (d50) and 58 μm (d90). The manufacturing experiments in this study consist of three builds containing identical specimens with invariable cross-sections. The builds are differentiated by the nominal layer thickness employed. The process parameters employed in manufacturing have been previously optimized for the attainment of a material containing a minimal amount of porosity through a design of experiments and metallographic evaluation of test coupons. The laser parameters used are in the transition between keyhole and conduction modes, to maximize the melt pool dimensions while avoiding keyhole instability and systematic keyhole porosity [28]. To verify that the parameters yield virtually defect-free material, small test coupons were manufactured in prints where the effect of spatter redeposition was deemed negligible, and characterized following the procedure described in our previous work [28]. In short, the internal defects were characterized via image analysis of a cross-section of approximate dimensions 20 mm × 10 mm. The results are documented in the Appendix.

The manufacturing process was conducted in an argon atmosphere with a maximum oxygen content of 0.1 %. The gas flow settings were kept constant throughout the builds, with exposure order against the gas flow direction. The build layout is schematized in Fig. 1, where the specimens analyzed in this study are represented in orange. The same three out of the five specimens from each build were analyzed.

2.2. In-situ monitoring and spatter detection

EOSTATE Exposure OT (EOS GmbH Electro Optical Systems, Germany) was used to monitor the build processes. In this monitoring system, a 5-megapixel sCMOS (scientific complementary metal-oxide-semiconductor) camera is installed on the outer top part of the build chamber and includes the entire build area in its field of view. The camera is equipped with a bandpass filter of 900 nm ± 12.5 nm, thus allowing acquisition within a narrow window of the near-infrared spectral range. During the exposure of each layer in the build process, the camera sequentially acquires images with the shutter time set to 0.1 s. The images registered during the laser exposure of a layer are then
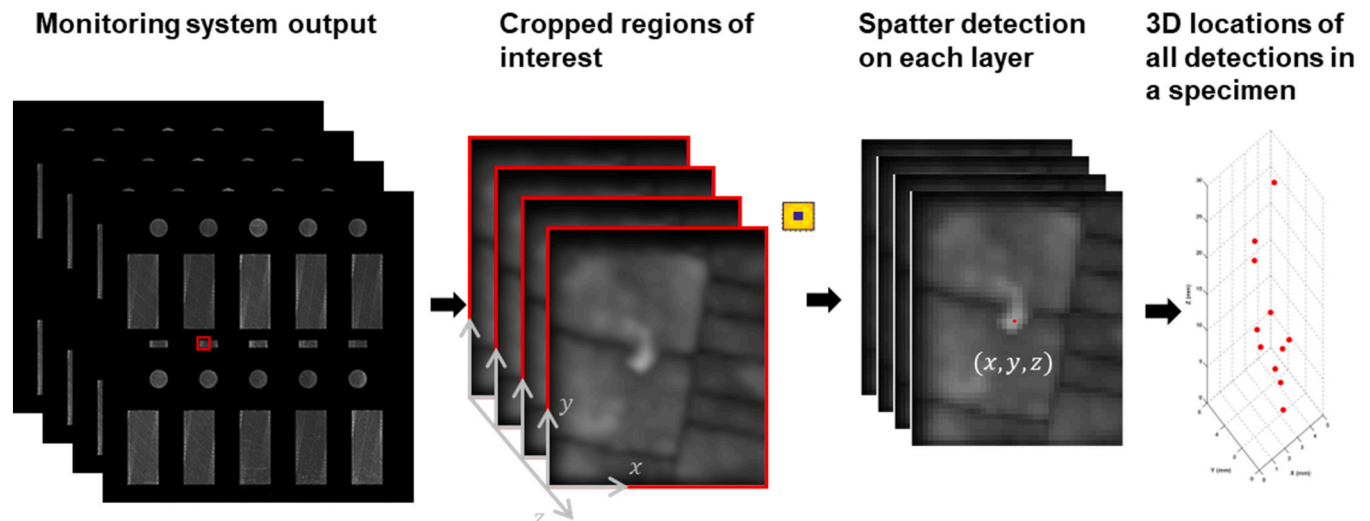

Fig. 2. Workflow for spatter detection from optical tomography process monitoring data.

Table 1

Number of lack of fusion defects and volume fraction of defects identified in the test specimens by XCT. The variable process parameters and the average remelt ratio are indicated. Laser power and hatch spacing are kept constant at 370 W and 100 μm, respectively.

Specimen ID	Laser scan speed (mm/s)	Nominal layer thickness (μm)	Average remelt ratio	Volume fraction of defects (%)	Number of gas pores	Number of lack of fusion defects
1a	800	80	3.5	<0.01 %	251	0
1b	900	80	3.3	<0.01 %	64	0
1c	1000	80	3.0	<0.01 %	159	0
2a	800	120	2.3	<0.01 %	1026	2
2b	900	120	2.2	<0.01 %	437	4
2c	1000	120	2.0	0.01 %	495	16
3a	800	150	1.9	0.10 %	3347	131
3b	900	150	1.7	0.25 %	2358	327
3c	1000	150	1.6	1.10 %	3667	630

combined within the system to output an image representing the maximum intensity value in regions of the build area of size 125 μm × 125 μm (*MAX* output) and an image representing the integral emitted intensities in the same region (*INT* output). EOSTATE Exposure OT was used only for acquisition; all data processing and analysis was done in a Matlab R2021b environment. Henceforth, "OT" is used to refer to this monitoring system, and "OT images" to its *MAX* output.

To detect spatter redeposits on the specimens analyzed in this study, firstly the monitoring images were cropped to correspond to the volume measured via XCT. Then, an image analysis algorithm is applied to the cropped images. The algorithm detects bright blobs through convolution with a Laplacian of Gaussian filter followed by non-minimum suppression. This approach is well-established in image analysis [29–31] and has also been used in prior work [8] for this specific type of image and application. The algorithm outputs the (x, y, z) coordinates of the detected spatter within the specimen, with z being a multiple of the nominal layer thickness. Fig. 2 schematizes the detection workflow.

2.3. X-ray computed tomography

The samples were inspected on a custom-developed X-ray CT system consisting of a microfocus X-ray tube (XWT-190-TCNF, X-RAY WorX), a 4000×4000 px^2 digital X-ray detector (XRD 1611 CP3, Perkin Elmer), and air-bearing motion axes [32,33]. Since Hastelloy X has a high X-ray absorption coefficient, the samples were cut to $5 \times 6 \times 29$ mm^3 to enable X-ray transmission in all scan directions. The X-ray tube was operated at a voltage of 190 kV and 20 W target power using a 1.0 mm copper filter to harden the spectrum. 5801 projections with an integration time of 4.0 s each and 2×2 pixel binning were recorded on a helical trajectory (1044° scan angle, 13.1 mm pitch). Projection data were beam hardening corrected and reconstructed into a volume consisting of $1700 \times 1700 \times 5600$ voxel with a voxel size of 5.1 μm using Siemens CERA 5.1.

XCT data analysis was performed in VG Studio MAX 3.4 (Volume Graphics). The volume data were filtered with a $3 \times 3 \times 3$ median filter and the outer sample surface was segmented using a gradient-based surface determination algorithm. Three perpendicular faces of the sample were used to create a local coordinate system for registration. Subsequently, a porosity analysis was performed using the VGEasyPore module with sub-voxel accuracy, a relative threshold of 35 % and a local area of 10 voxel to determine the local contrast. To render the XCT analysis more robust, defects were omitted if either the probability threshold (a non-disclosed quality metric) was below 0.1 %, the defect closer than 0.1 mm to the outer sample surface, or the defect size below 27 voxel, representing an equivalent diameter of 0.019 mm. Previous simulations confirmed that the recall rate, i.e. probability of detection, was close to 100 % and the false discovery rate close to 0 % when using these filter parameters, rendering the XCT data an appropriate ground truth [34]. For further analysis, volume slices were exported with a lateral resolution of 5.1 μm and a layer spacing corresponding to the build layer thickness (0.08 mm, 0.12 mm or 0.15 mm).

### 2.4. Microstructural analysis

Microstructural analysis was conducted on the specimens post-XCT. The preparation was performed with the following steps: mounting in epoxy resin, plane grinding with 320-grit sandpaper, fine grinding with 9 μm diamond suspension on a Struers MD-Largo surface, and polishing with colloidal silica. Etching was done electrolytically at 6 V in a solution of 5 g oxalic acid in 95 mL reagent grade HCl. The investigation was performed in the adjacencies of defects using a field emission gun scanning electron microscope (FEG-SEM) Leo Gemini 1550 (Carl Zeiss Microscopy GmbH). Additionally, the topmost layer of the specimens was examined for measurement of melt pool dimensions by means of light optical microscopy (LOM) using a Zeiss Axioscope 7 (Carl Zeiss Microscopy GmbH). A cross-section perpendicular to the scan vectors on that layer was analyzed, with 30 measurements performed per processing condition.

2.5. Matching X-ray computed tomography and in-situ monitoring data

As the coordinate systems for XCT measurements and OT images were dissimilar, with distinct origins and units, a coordinate transformation was performed. The bottom left corner of each analyzed specimens, as seen in OT images, of the first manufacturing layer was assigned as the origin, see Fig. 2. The conversion from pixels to metric units was obtained in the xy plan by multiplying by 125 μm, which corresponds to a pixel in OT images. In the z direction, the layer number was multiplied by the nominal layer thickness to obtain the z position in metric units. As the post-processing step of cutting the specimens from the build platform results in a loss of around 1 mm of material, the z coordinates were adjusted to match the location of the top labels as the maximum z in both OT images and XCT. With that, the first OT images, corresponding to the material lost in the cutting process and not measured via XCT, were discarded. Next, the XCT detections were clustered into lack of fusion and porosity. After that, a point-by-point comparison of the detections obtained from the two systems was performed to assess the performance of the OT system combined with the image analysis approach to detect spatter-induced lack of fusion.

3. Results and discussion

All processing parameters used in this study, previously optimized to yield a material with minimal porosity, are indicated in Table 1. From previous studies [8,14], it is known that the number of spatter-driven defects within a specimen is sensitive to its position in the build area, in particular to the distance to the gas outlet. In this study, the distance of the specimens to the gas outlet is invariable, and the effect of other factors on spatter-driven defect formation is investigated. More specifically, due to the variation of the process parameters, the melt pool morphology and dimensions in each specimen differ, as well as the remelt ratio, defined as the ratio between average melt pool depth and nominal layer thickness. The average remelt ratios calculated from the
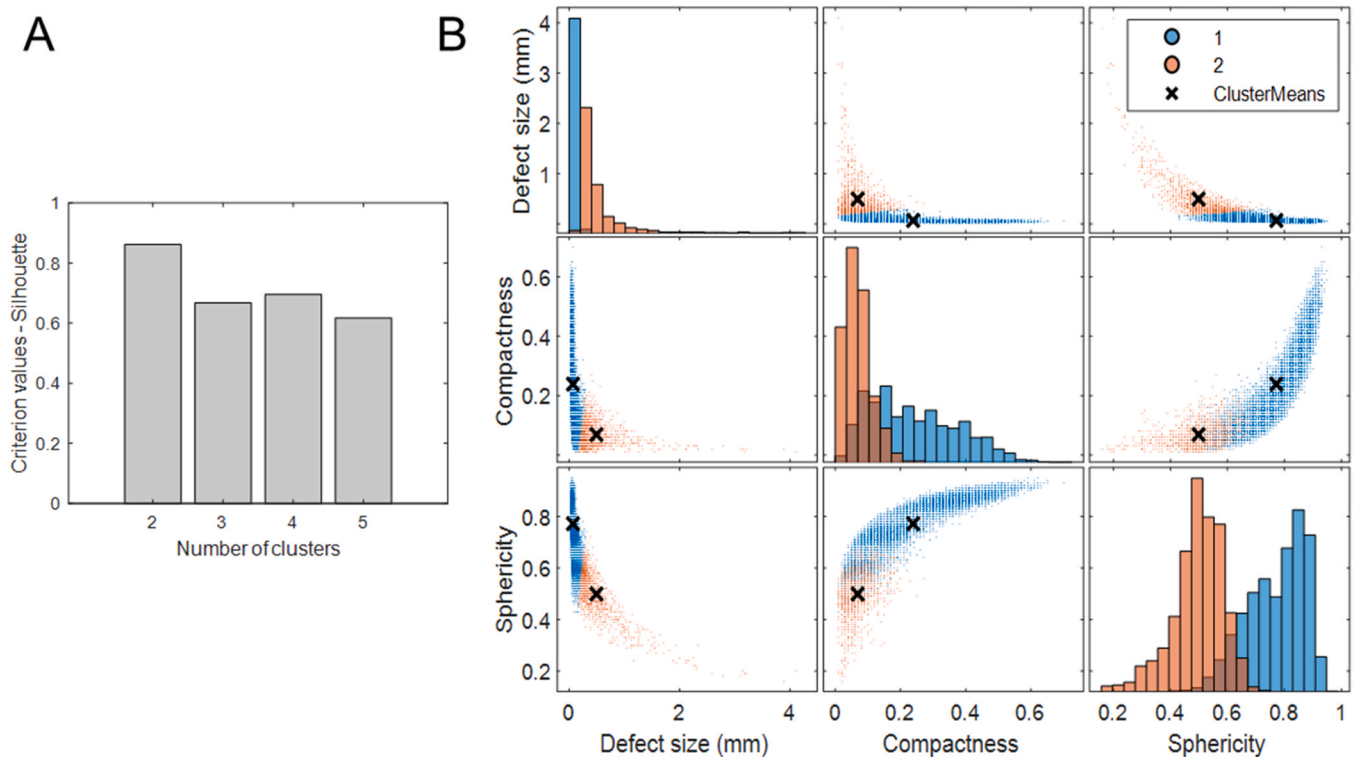
Fig. 3. A) Evaluation of the optimal number of clusters via the silhouette evaluation criterion B) Scatterplot matrix visualization of clusters of defect data. The distributions of the variables used for clustering (defect size, compactness, and sphericity) are represented as histograms.

melt pool depth measurements divided by the nominal layer thicknesses are listed in Table 1.

3.1. Clustering of ground-truth defect data from X-ray computed tomography

Even though the processing parameters used in this study have been previously optimized to yield virtually defect-free material, the coupons were manufactured in builds with a high build area utilization [35], i.e., densely packed. This experimental layout increases the overall spatter generation due to the increased interaction of the laser beam with the powder bed, thus increasing the likelihood of spatter redeposition on the parts and their susceptibility to spatter-induced lack of fusion. As a result, the only defects expected within the material in this study are pores in small quantities, as observed in the test coupons used for verification of process parameters (see Appendix), and spatter-induced lack of fusion. Because the formation mechanisms of these defect types are dissimilar [4,36,37], and spatter-induced defects are the object of this study, the detection of pores is outside the scope. Thus, the detections obtained via XCT scan must be separated per type, so only lack of fusion defects are further analyzed.

To differentiate defects detected by XCT according to their type, clustering was performed. Three variables contained in the XCT data were considered: defect size, measured as the diameter of the circumscribed sphere of the defect; sphericity, defined as the ratio between the surface of a sphere with the same volume as the defect and the surface of the defect; and compactness, defined as the ratio between the volume of the defect and the volume of the circumscribed sphere.

Clustering was performed via k-means clustering. Firstly, a clustering evaluation was performed to determine the optimal number of clusters in the dataset using the silhouette evaluation criterion [38]. The silhouette coefficient is a measure of similarity of a point to other points in its cluster compared to points in other clusters. A high silhouette value indicates that a point matches its cluster well and others poorly. The clustering solution is appropriate if most points have a high silhouette

value. Fig. 3A shows the sum of all silhouette values for 2–5 clusters and confirms that the optimal number of clusters is two. The clustering of the 12,914 XCT defect data points from all specimens can be visualized in the matrix of plots in Fig. 3B. The three variables used for clustering are plotted in three combinations of two as scatterplots, where it is possible to visualize the patterns of each cluster. Additionally, each of the variables is represented in a histogram format, where the values assumed by each of the two clusters are also distinguished by color. Cluster 2 (in orange) corresponding to around 9 % of all defects, but 94 % of the total volume of defects, is characterized by larger defects with lower compactness and sphericity. Low sphericity values combined with large defects have previously been listed as a characteristic of lack of fusion defects [39,40]; therefore, the defects in cluster 2 will be henceforward referred to as lack of fusion, and the defects in cluster 1 as pores.

The defect population in each specimen separately is observed in Fig. 4, where pores and lack of fusion are represented in black and red, respectively. The scales are kept constant across plots for easier comparison. Note that a logarithmic scale was used on the *x*-axis, representing defect size. As the processing conditions become less robust, i.e., with a lower remelt ratio, the presence of large (mm-sized) lack of fusion defects becomes common. Note that no lack of fusion defects were observed in the specimens manufactured with a nominal layer thickness of 80 μm (1a – 1c), which indicates robustness of this processing condition to spatter-induced defect generation. When a nominal layer thickness of 120 μm was used, a few lack of fusion defects were observed, and the sensitivity to varying remelt ratios is clearly observed. For the largest nominal layer thickness (150 μm), a large number of lack of fusion defects was observed for all three specimens (3a – 3c), and both their quantity and size scales with decreasing remelt ratios. Despite that, the volume fraction of defects, based on XCT measurements, is relatively low for all specimens, as observed in Table 1, thus highlighting the shortcomings of relative density as a quality metric in LPBF [28].

Table 1 clearly shows that for sufficiently large remelt ratios (3 and above), XCT detected no lack of fusion (defects in cluster 2). For smaller remelt ratios, the number of lack of fusion defects scales with the
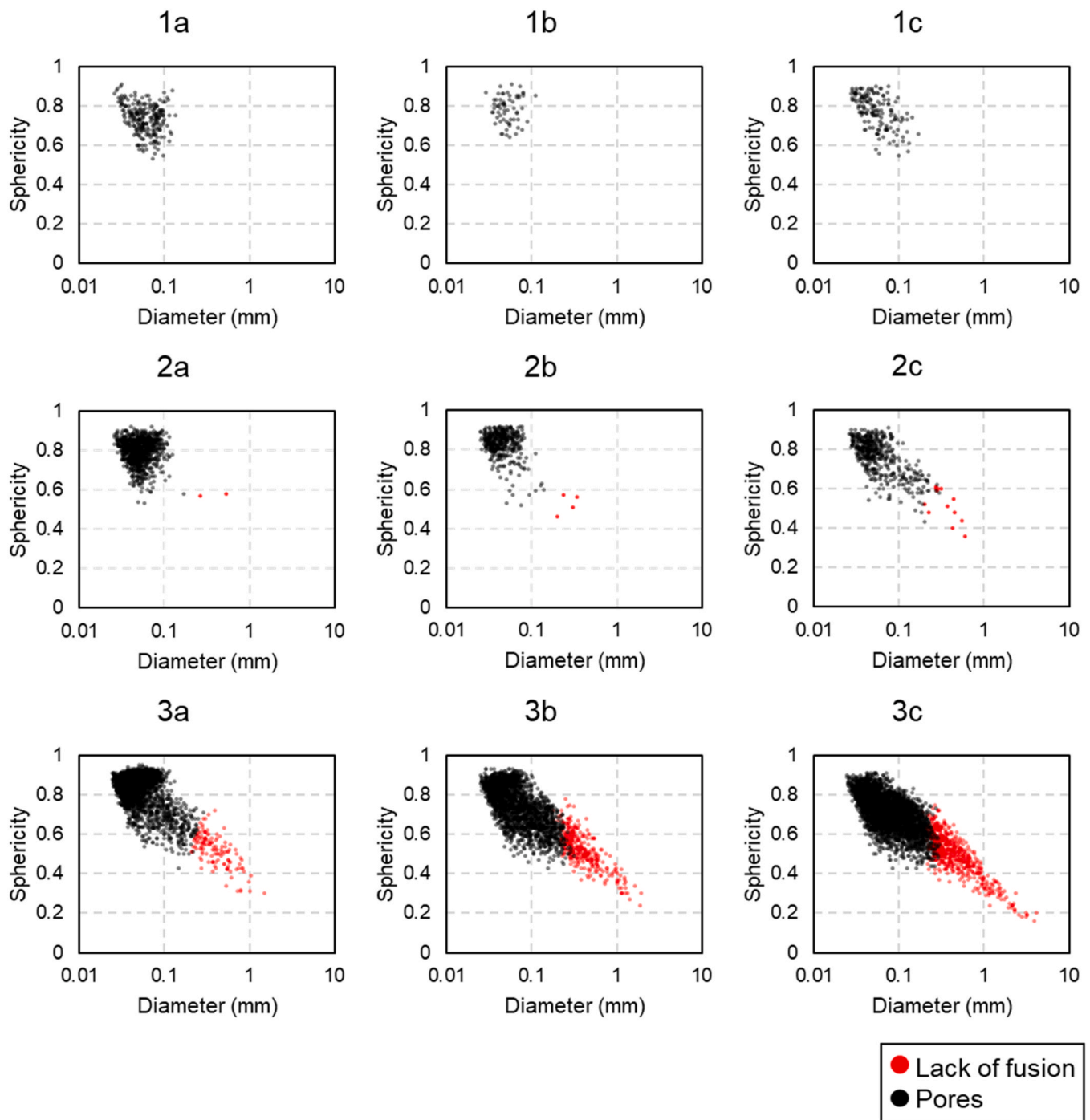
Fig. 4. Representation of the internal defects detected via XCT in each individual specimen. Red points denote lack of fusion defects; black points denote pores.

decrease in remelt ratios down to a factor of approximately 2, where a breaking point is reached, and the number of lack of fusion defects increases rapidly. These results indicate that differences in defect populations are due to the varying robustness of the processing conditions, i. e., to their varying sensitivity levels to spatters driving lack of fusion. This conclusion is in accordance with Taheri Andani et al. [41], who observed that even though a decrease in laser power input reduces the number of spatter particles generated, it prompts an increase in the defect percentage within the material.

3.2. Microstructural analysis

Microstructural investigation of the specimens shows that the porosity present in the specimens is predominantly residual gas porosity (represented by white arrows in Fig. 5), but some keyhole pores (represented by red arrows in Fig. 5) are also occasionally observed.

Microstructural investigation also reveals particles on the surface of the parts in manufacture (Fig. 6 A and B). The particles can be incorporated into the material upon manufacture of subsequent layers (Fig. 6 C and D), notably when the remelt ratio is larger, or can fail to be incorporated in the material upon manufacture of subsequent layers, presumably originating lack of fusion (Fig. 6 E, F and G), as previously observed in other studies [13,23,42]. The interaction of a single particle with the laser beam can either result in its incorporation into the bulk material (C) or in insufficient binding (E and G). The same observations are valid for the interaction of a cluster of particles with the laser beam,
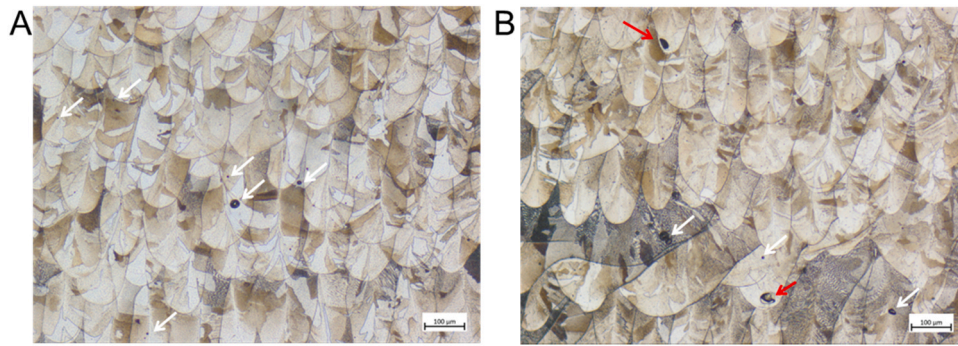
Fig. 5. Microstructure of specimens 2b (A) and 3b (B), highlighting the porosity present. Residual gas pores are indicated by white arrows; keyhole pores, by red arrows.
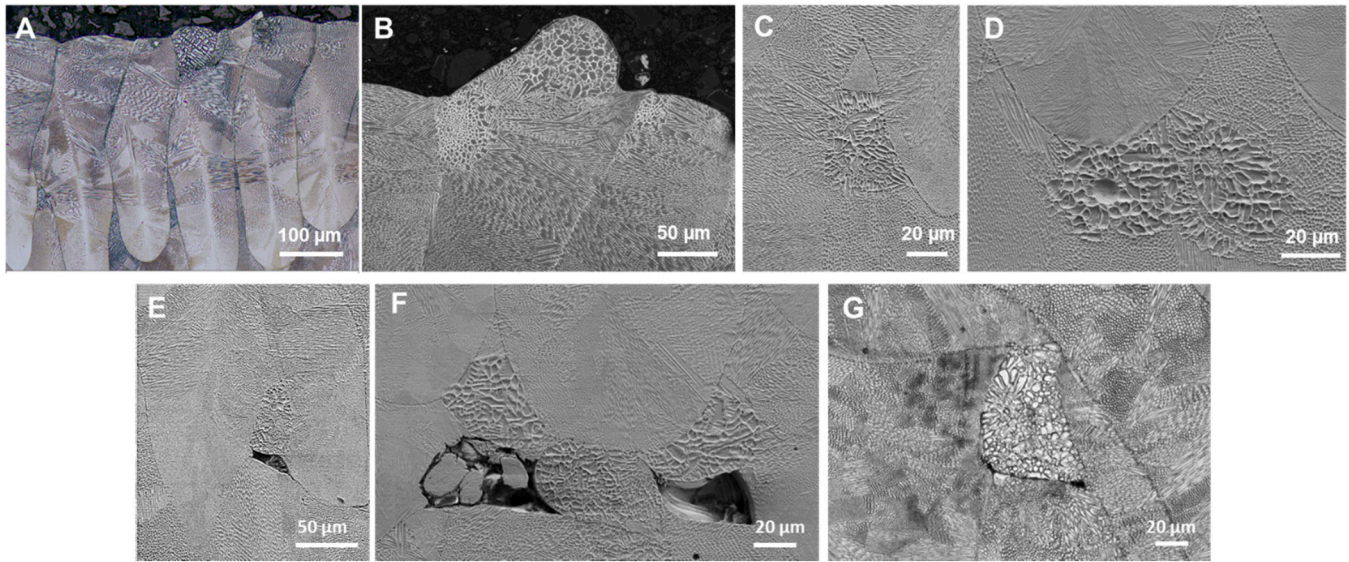

Fig. 6. Interactions of spatter particles with the bulk material. Particles deposit on the surface of the material (A, B) and can be incorporated into the bulk during future interactions with the laser (C, D). Complete fusion can be prevented due to the presence of spatter particles (E-G).
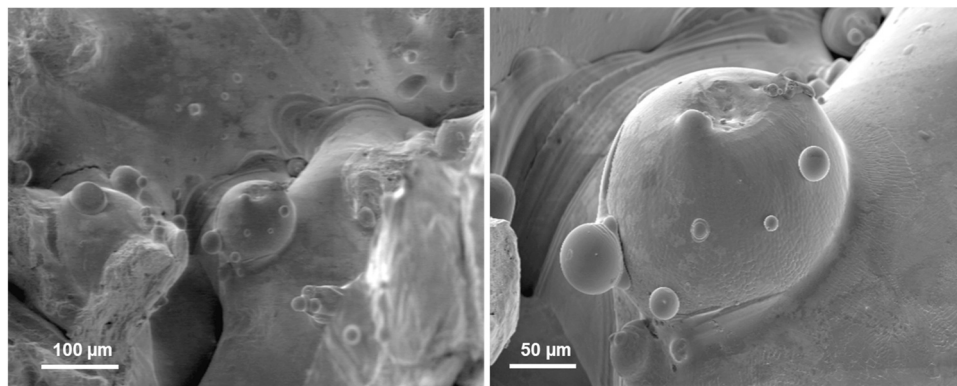

Fig. 7. Fracture surface of specimen 3c. The smooth surface is presumed lack of fusion. Multiple particles are observed on its surface, among them a particle with diameter of around 120 μm and multiple satellites.

as illustrated in D and F. It is not trivial to ascertain that the particles observed consist of spatter. Spatter particles differ from feedstock particles mainly in size and surface characteristics [8,10–13]. The particle size being larger than the feedstock is indicative that the particle was generated in-process; however, a large portion of generated spatter particles is within the size range of the feedstock [8,11]. Additionally,

the sizes measured in cross-sections do not necessarily correspond to the maximum particle size, making this criterion less than ideal to determine the nature of a particle. Spatter particles are typically covered with an oxide layer substantially thicker than that present on the virgin powder, on average [8,12,43]. However, there are substantial particle-to-particle variations, and, while the largest particles tend to be
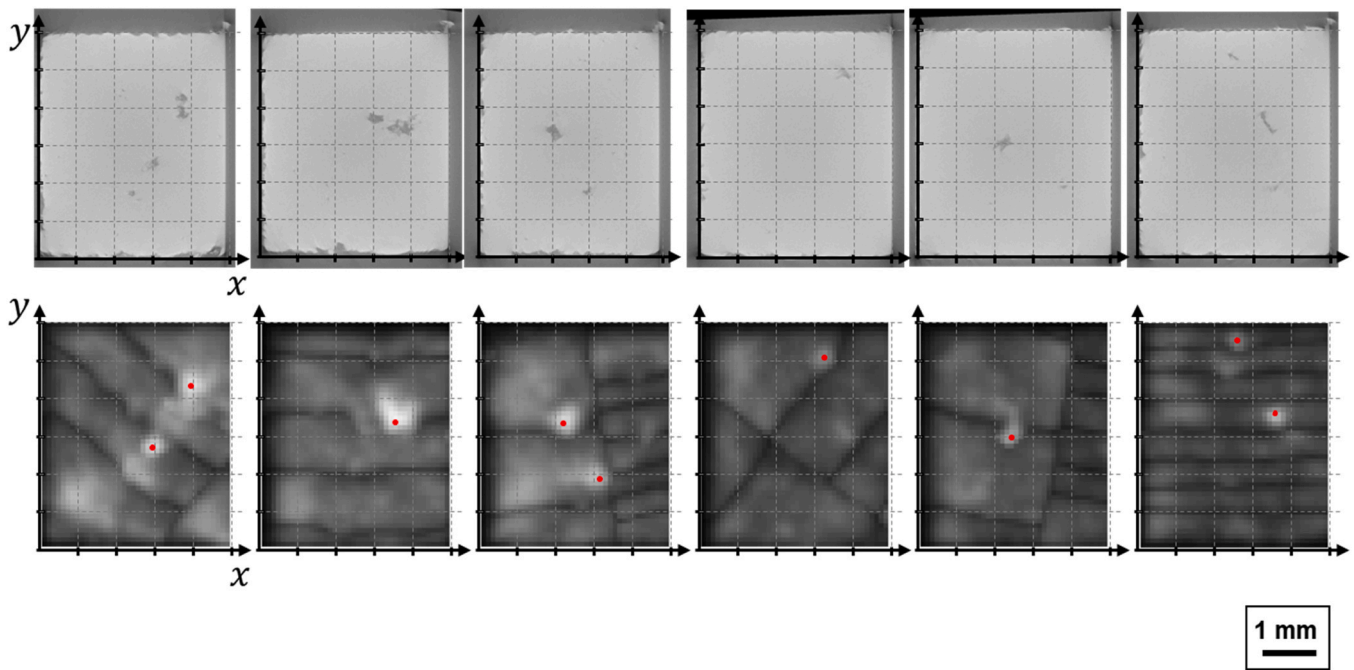
Fig. 8. Visual correspondence between XCT slices (top) and OT images overlaid with detections (bottom). A coordinate system and a grid are superimposed on the images for better visualization of the locations of lack of fusion in XCT and detections in OT images.
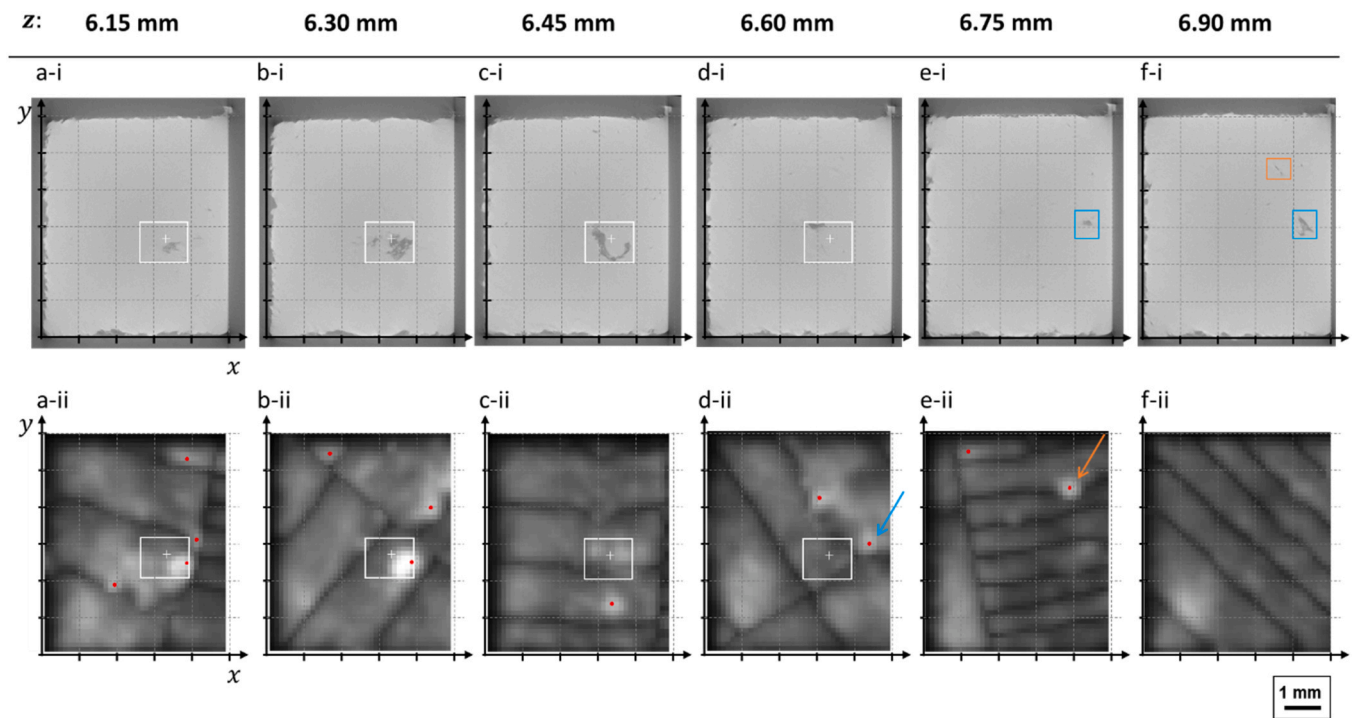

Fig. 9. A large lack of fusion in specimen 3a that extends through four printing layers. The XCT slices are seen on the top row, and the corresponding OT images are seen on the bottom row, overlaid with detections represented by red dots. All images are overlaid with the (x, y) center of the defect, represented by a cross, and its projection in the (x, y) plan, represented by the box. The build height is indicated in mm. The blue arrow indicates a detection associated with another major lack of fusion, visible in subsequent XCT slices.

covered with thicker oxide layers [43], this thickness is in the order of a couple of hundreds of nanometers, maximum. In this study, the surface oxide layer could not be distinguished on the cross-sections by energy dispersive X-ray spectroscopy (EDX).

Therefore, the determination of whether a given particle observed in a cross-section is spatter is challenging. On the other hand, observation

of the particles on a free surface allows a more accurate measurement of particle size and observation of surface characteristics. Specimen 3c, which contains abundant lack of fusion defects, was manually fractured to investigate a typical lack of fusion defect by direct observation from a perspective alternative to the cross-sections exemplified in Fig. 7. The fracture surface in Fig. 7A reveals multiple particles attached to a

Table 2
Evaluation metrics when the spatter detection method is applied to each specimen separately and compared to ground-truth XCT data.

Specimen ID	TP	FP	FN	Precision $\frac{TP}{TP+FP}$	Recall $\frac{TP}{TP+FN}$	False negative rate $\frac{FN}{FN+TP}$	False discovery rate $\frac{FP}{TP+FP}$	F1 score $\frac{2TP}{2TP+FP+FN}$
1a	0	68	0	-	-	-	-	-
1b	0	12	0	-	-	-	-	-
1c	0	0	0	-	-	-	-	-
2a	2	22	0	0.08	1.00	0.00	0.92	0.15
2b	2	6	2	0.25	0.50	0.50	0.75	0.33
2c	5	8	11	0.38	0.31	0.69	0.62	0.34
3a	120	41	11	0.75	0.92	0.08	0.25	0.82
3b	254	10	73	0.96	0.78	0.22	0.04	0.86
3c	494	0	136	1.00	0.78	0.22	0.00	0.88
Overall	**877**	**167**	**233**	**0.84**	**0.79**	**0.21**	**0.16**	**0.81**

smooth surface, presumably lack of fusion. The measured particle diameters are typically up to 50 μm and, due to their size, can either be smaller spatter or feedstock particles. Larger particles were occasionally observed. For example, Fig. 7B depicts a particle of diameter ~120 μm with multiple satellites, most likely a spatter particle due to its dimensions, significantly larger than the feedstock powder. The particle presents patches of oxide on the surface, corroborating the claim that it is spatter.

3.3. Detection of redeposited spatter particles on optical tomography images acquired in-situ

A visual comparison between corresponding XCT volume slices and OT images overlaid with spatter detections is provided in Fig. 8, where a grid with 1 mm spacing is superimposed on both sets of images. These instances have been randomly selected from several specimens. The correspondence between spatter detections and defects is evident, especially for larger defects. A fair spatial correspondence between both detections is present, but the match is not exact, as the features detected are distinct (voids for XCT and spatters for OT). As spatter particles induce defects, a slight offset is expected and observed.

Defects can extend to several layers of the build, notably in the form of large lack of fusion. Fig. 9a-d shows XCT and OT image representations of the largest lack of fusion present in specimen 3a. This defect has a measured size of 1.483 mm and a projected size of 0.608 mm in the z-direction, meaning it spans approximately four layers. The XCT image slices are overlaid with the 1-mm spaced grid and with the center of the XCT detection, represented as a cross, and with the projections in x and y directions, represented by a box. Two OT images in the corresponding layers contain detections within the bounding box of the defect (a-ii and b-ii), and the first one contains additional detections in its vicinity. In the subsequent OT images (c-ii and D-ii), further detections appear in the adjacencies of the bounding box, possibly as a manifestation of disturbances associated with the newly formed defect. In Fig. 9a-d, the only other detection associated with another major defect is indicated with a blue arrow. This second defect is visible in the next XCT slices and is marked with a blue box in Fig. 9e-i and f-i. In Fig. 9e-ii, another distinct detection is visible (indicated by the orange arrow) and is in the vicinity
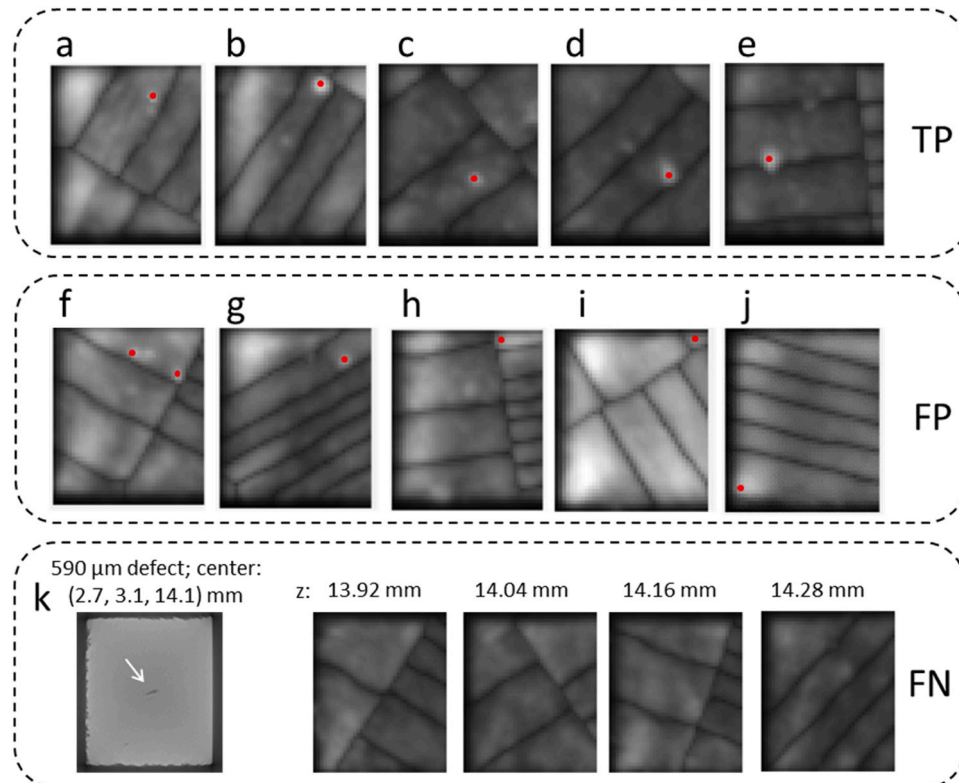

Fig. 10. Examples of true positive (TP) occurrences (a-e), false positives (FP) (f-j), and a false negative (FN) (k).
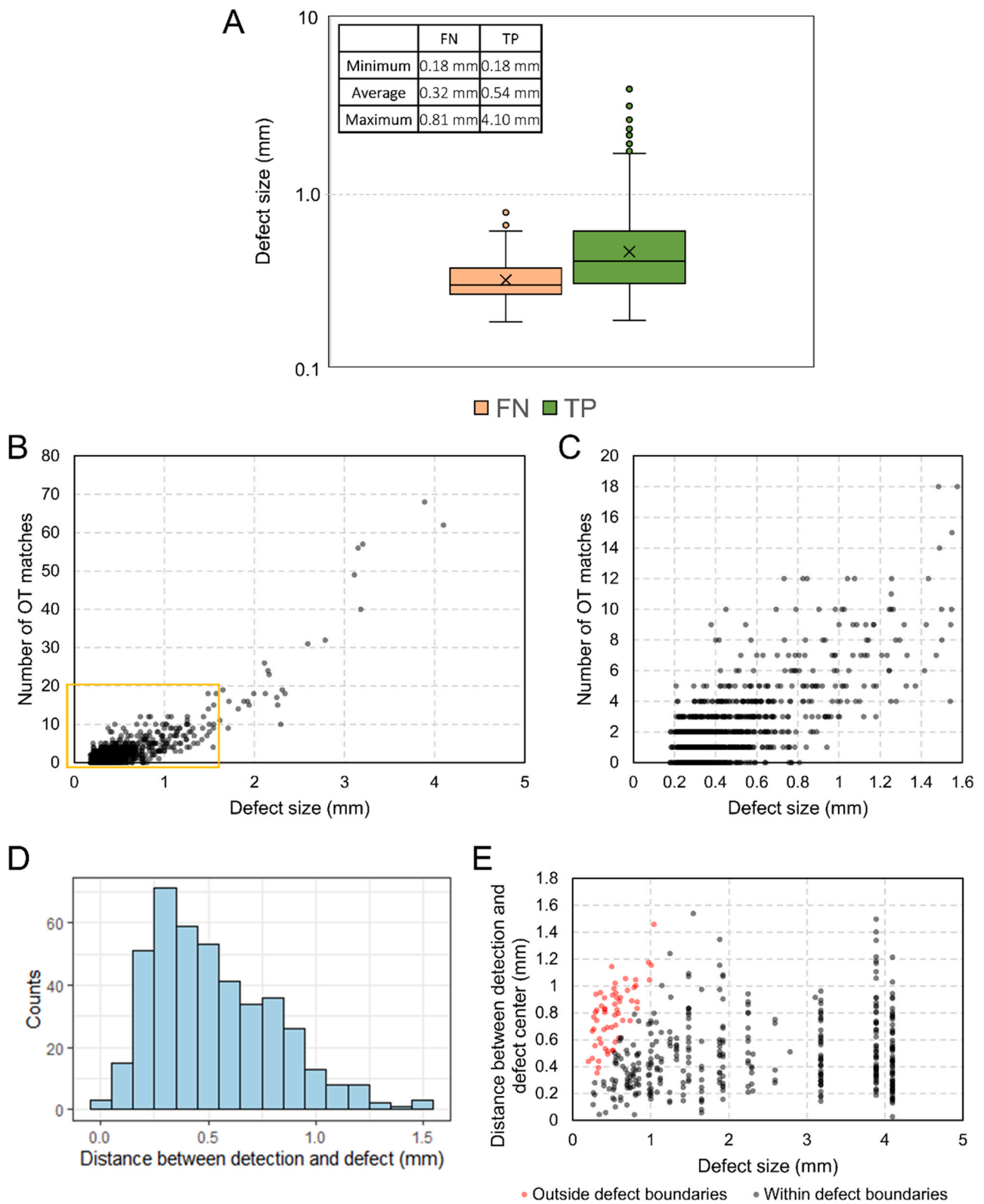
Fig. 11. Analytics of matches of detections in OT images and defects measured via XCT. A: Sizes of lack of fusion defects detected simultaneously via XCT and OT (TP), and not detected via OT (FN). The table insert shows the minimum, average, and maximum defect sizes in each category, FN and TP. B and C: Number of detections in OT images matching a single defect, plot against its size. C Illustrates a magnification of the range with the most occurrences, represented by the yellow box in B. D: Distribution of the distances between the center of TP OT detections and the center of lack of fusion, measured by XCT. E: Distance between detections and defect centers plot against the defect size.

of a third large defect, highlighted in Fig. 9f-i by an orange box.

In general, spatter particles will be visible in OT images due to their near-infrared emissions overlapping the range of acquisition of the sensor. The spectral radiance emitted is higher with higher temperatures, according to Planck's law. However, cooling rates in LPBF can range between 1 and 40 K/μs [44]. Considering that in the OT system, an extended shutter time (100 ms) is used, the intensity observed in OT images is predominantly providing information on the local heat transfer. The interaction of the laser beam with the feedstock and possibly spatter particles causes the particles to melt, and the melted region to be visible (have a nonzero intensity) in OT images. With the disturbance provoked by, e.g., spatter particles in the fusion zone, the heat provided by the laser beam might not be effectively transferred due to insufficient connection of the particle with the remaining material, resulting in local accumulation and an afterglow, or bright blob, in OT images. As observed in previous work [8], these detections occur almost exclusively in areas actively used for manufacturing. This observation suggests that the local signal peak resulting in a detection is predominantly a result of the interaction of hot spatter particles with the laser beam rather than purely the radiance emitted by the particles.

3.4. Matching ex-situ X-ray computed tomography and in-situ optical tomography detections

The XCT data analysis outputs key features of each detected defect, among which the diameter $d_{ct,i}$ and the $(x_{ct,i}, y_{ct,i}, z_{ct,i})$ coordinates of the center position of the sphere circumscribing the defect i, also referred to as "defect center" in this study. Considering the offset between the position of spatter detection j and defect i, and that the z output of detections in OT images is a multiple of the nominal layer thickness t, Eq. (1) was formulated as the matching criterion.

$$\sqrt{\left(x_{s,j} - x_{ct,i}\right)^2 + \left(y_{s,j} - y_{ct,i}\right)^2 + \left(z_{s,j} - z_{ct,i}\right)^2} \le d_{ct,i} + t + e \quad (1)$$

Where $\left(x_{s,j}, y_{s,j}, z_{s,j}\right)$ are the coordinates of the center position of the spatter particle j, and e is an error factor corresponding to 0.5 mm, which accounts for deviations such as the size of spatter particles (up to 0.2 mm, as measured in [8]), and the (x, y) mismatch observed in Fig. 8 and Fig. 9. Additionally, the matching of the coordinate systems is a source of error in itself. The resolution of the OT system is a limitation, as each pixel corresponds to an area of 125 μm × 125 μm in the xy plan, and of the nominal layer thickness in the z direction. Further, in the z direction, it is assumed that the nominal layer thickness equals the effective layer thickness, while a mismatch actually exists between the two [45,46].

Thus, a spatter detection j in an OT image matches a defect i if the criterion above is met, and in this case, the detection is a true positive (TP). Note that it is possible and likely that multiple detections in OT images match a single defect (XCT detection) because a disturbance can propagate through multiple layers, as illustrated in Fig. 9, and because multiple spatters landing close together can create a massive 3D defect. Spatter detections in OT images that do not meet the criterion above, i. e., do not match a lack of fusion indicated by XCT, are false positives (FP). Lack of fusion defects detected by XCT that do not have at least one match in OT images are false negatives (FN).

Table 2 summarizes the evaluation of the detection method proposed in this work. False positives were found consistently in most specimens. Their presence can partially be explained by the incorporation of the particle into the bulk and by the iterative nature of the process, which prompts remelting of the top layers and allows defects to heal. Part of the FP detections has the same characteristics as TP detections, as observable by comparing the FP in Fig. 10 f-g with the TP in Fig. 10 a-e, which indicates that spatter redeposited in this location and was subsequently fully incorporated into the bulk, not forming a defect. Part of the FP detections has a distinct appearance, as illustrated in Fig. 10 h-j (and

even visible in Fig. 9a-ii, b-ii, and e-ii). In these cases, the laser exposure pattern and short scan vectors provoke the emergence of brighter regions, as previously reported in the literature [47]. The higher local intensity combined with the surrounding darker features, i.e., specimen edges and stripe overlaps, result in detections, despite the dissimilarity of these regions to the features of interest. The resulting occurrences of FP have a higher representativity in specimens manufactured with a higher global energy input (1a and 1b). Because these FP are concentrated on the edges of the specimens, an alternative to improve the detection method is discarding edge detections in processing conditions with high energy input. In this study, the detection parameters were deliberately kept constant to enable the recognition of such patterns. Overall, the performance of the algorithm can be expected to increase if adjustments such as sensitivity and edge detections are tailored to each process setting.

With the FP and TP of all specimens summed, the overall false discovery rate is 16 %, which implies that the overall precision is 84 %. Within the same group (same nominal layer thickness), the number of FP tends to scale with the increased remelt ratio, and the inverse trend is observed for TP, mainly due to fewer lack of fusion occurring with an increased remelt ratio, as shown in Table 1. Consequently, the precision decreases and the false discovery rate increases with more robust processing conditions. On the other hand, specimens with a higher remelt ratio are less prone to false negatives, i.e., it is less likely to miss an existing defect in specimens manufactured with more robust processing conditions. Fig. 10k exemplifies an FN occurrence in specimen 2c. The XCT slice where the defect is visible is shown, together with its coordinates and size. The OT images representing the layers closest to the z coordinate of the defect center do not contain any features of interest, indicating that the occurrence of FN is not due to a fault in the detection algorithm. The overall false negative rate, considering the sum of all FN and TP throughout the specimens, is 21 %, meaning 79 % of the defects are detected. For the *overall* evaluation of the method in Table 2, TP, FP, and FN are summed across specimens, and the deriving metrics are calculated based on these sums. It is noteworthy that the overall evaluation metrics do not consider each specimen equally, and their contribution is weighted based on their individual numbers of TP, FP, and FN.

The count of FN is particularly substantial in specimens manufactured with a nominal layer thickness of 150 μm (3a–3c). The lack of fusion defects in these specimens might have alternative origins to spatter redeposition. Locally inhomogeneous powder packing is a well-known stochastic defect-inducing factor [4,48,49] that is likely present in these specimens due to the irregularities caused by the large number of spatter redeposits. Thus, the formation of defects observed in this study, particularly in specimens 3b and 3c, is plausibly a result of two defect-inducing stochastic processes occurring simultaneously, of which only one is detectable through the method proposed here.

With the method proposed in this study, the largest defects within the specimens were successfully detected, as seen in Fig. 11A. Additionally, it is observed that the defects not detected in OT images (FN) tend to be smaller than the ones successfully detected (TP). Fig. 11B confirms that the largest defects tend to be detected multiple times. Notably, defects over 3 mm are associated with a minimum of 30 detections. Defects in the size range more often observed are highlighted in Fig. 11C, where it is also observed that the number of detections tends to scale with defect size. Fig. 11D shows the distance of the centers of TP detections in OT images to the centers of the circumscribed spheres of corresponding defects. The range 0.3–0.4 mm contains the most occurrences, while the average distance is 0.53 mm. Only a few observations presented a distance of less than 0.1 mm, which is a critical aspect to consider when estimating the location of the spatter-induced defect. The distance between detections in OT images and the defect center after coordinate transformation is not related to the defect size, as illustrated in Fig. 11E. The distances between the largest defects and their multiple detections span a wide range. In Fig. 11E, it is also highlighted that many

Table 3

Summary of defect populations measured in coupons manufactured with each set of process parameters used in this study. The measurement was made via image analysis of a cross section of approximately 20 mm × 10 mm.

Parameter set ID	Laser power (W)	Laser scan speed (mm/s)	Hatch spacing (μm)	Nominal layer thickness (μm)	Volume fraction of defects (%)	Maximum defect size (μm)
1a	370	800	100	80	0.007	42
1b	370	900	100	80	0.005	38
1c	370	1000	100	80	0.006	42
2a	370	800	100	120	0.037	78
2b	370	900	100	120	0.019	88
2c	370	1000	100	120	0.024	36
3a	370	800	100	150	0.072	70
3b	370	900	100	150	0.049	43
3c	370	1000	100	150	0.066	88

detections are outside the defect boundaries, i.e., outside the sphere circumscribing the defect. Detections outside defect boundaries are more prevalent for defects of size 1 mm or less, thus showing that the addends to defect size in Eq. (1), i.e., the error factor and the layer thickness, are essential to detecting defects in this size range.

4. Conclusions

This study addressed the in-situ detectability of spatters redeposits, responsible for defect formation in laser powder bed fusion. Hastelloy X specimens were measured via XCT, and the lack of fusion defects detected were compared to those detected in images acquired via optical tomography (OT) in-situ monitoring. Variability was introduced in the experiment by different processing conditions that induce varying remelt ratios. The main findings are summarized as follows:

- No lack of fusion was identified through XCT in specimens manufactured with a remelt ratio of 3 and above, indicating that processing conditions that meet this criterion fully incorporate spatter in the bulk and are robust to spatter-induced defects. Conversely, remelt ratios below 2 have a high sensitivity to spatter-driven defects.
- A clear visual correspondence between detections in OT images and defects in XCT was observed. Some location offset is consistently observed and the distance between detections and defect centers averages 0.53 mm. The offset is attributed to the fact that the features detected are distinct (defects for XCT and spatters for OT images), with spatter particles potentially inducing defects.
- Multiple detections in OT images can be matched to a single lack of fusion, particularly if the defect is large enough to span multiple

build layers. The number of detections in OT images scales with the defect size.
- The method proposed here had a false discovery rate of 16 %, attributed to full incorporation of spatters into the bulk, and faulty detections on specimen edges due to short scan vectors.
- Considering all analyzed specimens, 79 % of lack of fusion defects were detected with the method proposed in this study. As the match between detections in OT images and XCT features varies substantially among specimens, the performance of the algorithm can be expected to increase if adjustments such as sensitivity and edge detections are made for each specific process setting.
- Manufacturing with robust processing conditions decreases the likelihood of missing an existing defect, i.e., of obtaining a false negative. On the other hand, it increases the likelihood of obtaining false positives using the method proposed in this study.
- Locally inhomogeneous powder packing may potentially act as an important alternative stochastic defect-inducing factor in specimens where a large number of spatter redeposits are detected, as the spatter particles introduce packing irregularities. The occurrence of this event simultaneously with spatter redeposition is a possible explanation for the considerable number of false negatives present in two of the specimens.

This study demonstrates that in-situ monitoring using optical tomography can be employed for indirect detection of stochastic lack of fusion through inference from the detection of spatter redeposits. The detectability of random, internal, and typically large defects in-process is a pivotal step towards their mitigation, achievable through closed-loop control to be developed in future work.
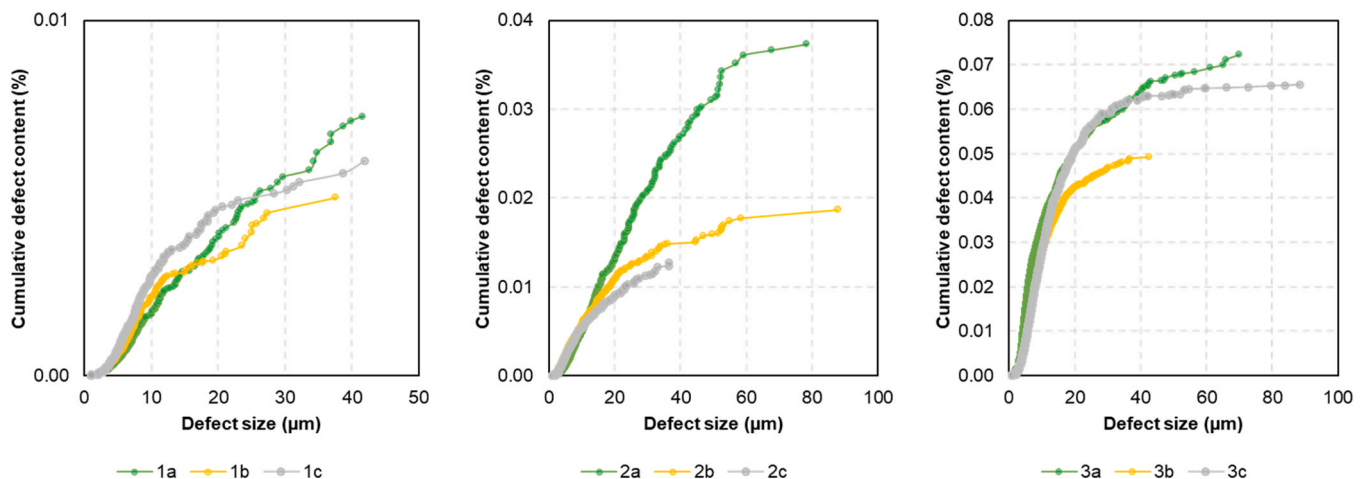

Fig. 12. Graphical representation of the defect populations obtained from each set of process parameters.

CRediT authorship contribution statement

Schwerz Claudia: Writing – original draft, Visualization, Validation, Software, Methodology, Formal analysis, Data curation, Conceptualization. **Bircher Benjamin A.:** Writing – review & editing, Methodology, Formal analysis, Data curation. **Küng Alain:** Writing – review & editing, Methodology, Formal analysis, Data curation. **Nyborg Lars:** Writing – review & editing, Project administration, Funding acquisition.

Declaration of Competing Interest

The authors declare the following financial interests/personal relationships which may be considered as potential competing interests: Lars Nyborg reports financial support was provided by Horizon 2020 European Innovation Council Fast Track to Innovation.

Data Availability

Data will be made available on request.

Acknowledgments

Appendix. A – Verification of the defect populations in test coupons manufactured with the intended process parameters

See Table 3 and Fig. 12.

References

[1] T.G. Spears, S.A. Gold, In-process sensing in selective laser melting (SLM) additive manufacturing, Integr. Mater. Manuf. Innov. 5 (2016) 16–40, https://doi.org/10.1186/S40192-016-0045-4.

[2] Y. AbouelNour, N. Gupta, In-situ monitoring of sub-surface and internal defects in additive manufacturing: a review, Mater. Des. 222 (2022), 111063, https://doi.org/10.1016/J.MATDES.2022.111063.

[3] S. Coeck, M. Bisht, J. Plas, F. Verbist, Prediction of lack of fusion porosity in selective laser melting based on melt pool monitoring data, Addit. Manuf. 25 (2019) 347–356, https://doi.org/10.1016/j.addma.2018.11.015.

[4] Z. Snow, A.R. Nassar, E.W. Reutzel, Invited review article: review of the formation and impact of flaws in powder bed fusion additive manufacturing, Addit. Manuf. 36 (2020), https://doi.org/10.1016/j.addma.2020.101457.

[5] E. Malekipour, H. El-Mounayri, Common defects and contributing parameters in powder bed fusion AM process and their classification for online monitoring and control: a review, Int. J. Adv. Manuf. Technol. 95 (2018) 527–550, https://doi.org/10.1007/s00170-017-1172-6.

[6] M. Grasso, V. Laguzza, Q. Semeraro, B.M. Colosimo, In-process monitoring of selective laser melting: spatial detection of defects via image data analysis, in: J. Manuf. Sci. Eng. Trans, 139, ASME, 2017, https://doi.org/10.1115/1.4034715.

[7] A. Ladewig, G. Schlick, M. Fisser, V. Schulze, U. Glatzel, Influence of the shielding gas flow on the removal of process by-products in the selective laser melting process, Addit. Manuf. 10 (2016) 1–9, https://doi.org/10.1016/j.addma.2016.01.004.

[8] C. Schwerz, A. Raza, X. Lei, L. Nyborg, E. Hryha, H. Wirdelius, In-situ detection of redeposited spatter and its influence on the formation of internal flaws in laser powder bed fusion, Addit. Manuf. (2021), 102370, https://doi.org/10.1016/J.ADDMA.2021.102370.

[9] Z. Li, H. Li, J. Yin, Y. Li, Z. Nie, X. Li, D. You, K. Guan, W. Duan, L. Cao, D. Wang, L. Ke, Y. Liu, P. Zhao, L. Wang, K. Zhu, Z. Zhang, L. Gao, L. Hao, A review of spatter in laser powder bed fusion additive manufacturing: in situ detection, generation, effects, and countermeasures, Micromachines 13 (2022), https://doi.org/10.3390/mi13081366.

[10] M. Simonelli, C. Tuck, N.T. Aboulkhair, I. Maskery, I. Ashcroft, R.D. Wildman, R. Hague, A study on the laser spatter and the oxidation reactions during selective laser melting of 316L stainless steel, Al-Si10-Mg, and Ti-6Al-4V, Metall. Mater. Trans. A Phys. Metall. Mater. Sci. 46 (2015) 3842–3851, https://doi.org/10.1007/s11661-015-2882-8.

[11] A.N.D. Gasper, D. Hickman, I. Ashcroft, S. Sharma, X. Wang, B. Szost, D. Johns, A. T. Clare, Oxide and spatter powder formation during laser powder bed fusion of Hastelloy X, Powder Technol. 354 (2019) 333–337, https://doi.org/10.1016/j.powtec.2019.06.004.

[12] A. Raza, C. Pauzon, E. Hryha, A. Markström, P. Forêt, Spatter oxidation during laser powder bed fusion of Alloy 718: Dependence on oxygen content in the process atmosphere, Addit. Manuf. 48 (2021), https://doi.org/10.1016/J.ADDMA.2021.102369.

[13] D. Wang, S. Wu, F. Fu, S. Mai, Y. Yang, Y. Liu, C. Song, Mechanisms and characteristics of spatter generation in SLM processing and its effect on the properties, Mater. Des. 117 (2017) 121–130, https://doi.org/10.1016/j.matdes.2016.12.060.

[14] R. Esmaeilizadeh, U. Ali, A. Keshavarzkermani, Y. Mahmoodkhani, E. Marzbanrad, E. Toyserkani, On the effect of spatter particles distribution on the quality of Hastelloy X parts made by laser powder-bed fusion additive manufacturing, J. Manuf. Process 37 (2019) 11–20, https://doi.org/10.1016/j.jmapro.2018.11.012.

[15] Y. Liu, Y. Yang, S. Mai, D. Wang, C. Song, Investigation into spatter behavior during selective laser melting of AISI 316L stainless steel powder, Mater. Des. 87 (2015) 797–806, https://doi.org/10.1016/j.matdes.2015.08.086.

[16] D. Wang, G. Ye, W. Dou, M. Zhang, Y. Yang, S. Mai, Y. Liu, Influence of spatter particles contamination on densification behavior and tensile properties of CoCrW manufactured by selective laser melting, Opt. Laser Technol. 121 (2020), 105678, https://doi.org/10.1016/j.optlastec.2019.105678.

[17] S. Hatami, Variation of fatigue strength of parts manufactured by laser powder bed fusion, Powder Met. (2021) 1–6, https://doi.org/10.1080/00325899.2021.2010932.

[18] H. Rieder, M. Spies, J. Bamberg, B. Henkel, On- and offline ultrasonic characterization of components built by SLM additive manufacturing, in: A.I.P. Conf. Proc., American Institute of Physics Inc, 2016, https://doi.org/10.1063/1.4940605.

[19] P. Lott, H. Schleifenbaum, W. Meiners, K. Wissenbach, C. Hinke, J. Bültmann, Design of an optical system for the in situ process monitoring of selective laser melting (SLM), Phys. Procedia 12 (2011) 683–690, https://doi.org/10.1016/J.PHPRO.2011.03.085.

[20] J.B. Forien, N.P. Calta, P.J. DePond, G.M. Guss, T.T. Roehling, M.J. Matthews, Detecting keyhole pore defects and monitoring process signatures during laser powder bed fusion: a correlation between in situ pyrometry and ex situ X-ray radiography, Addit. Manuf. 35 (2020), https://doi.org/10.1016/j.addma.2020.101336.

[21] R. McCann, M.A. Obeidi, C. Hughes, É. McCarthy, D.S. Egan, R.K. Vijayaraghavan, A.M. Joshi, V. Acinas Garzon, D.P. Dowling, P.J. McNally, D. Brabazon, In-situ sensing, process monitoring and machine control in Laser Powder Bed Fusion: a review, Addit. Manuf. 45 (2021), 102058, https://doi.org/10.1016/J.ADDMA.2021.102058.

[22] M. Grasso, A. Remani, A. Dickins, B.M. Colosimo, R.K. Leach, In-situ measurement and monitoring methods for metal powder bed fusion: an updated review, Meas. Sci. Technol. 32 (2021), 112001, https://doi.org/10.1088/1361-6501/AC0B6B.

[23] P.J. DePond, G. Guss, S. Ly, N.P. Calta, D. Deane, S. Khairallah, M.J. Matthews, In situ measurements of layer roughness during laser powder bed fusion additive manufacturing using low coherence scanning interferometry, Mater. Des. 154 (2018) 347–359, https://doi.org/10.1016/J.MATDES.2018.05.050.

[24] S. Keaveney, A. Shmeliov, V. Nicolosi, D.P. Dowling, Investigation of process by-products during the Selective Laser Melting of Ti6AL4V powder, Addit. Manuf. 36 (2020), 101514, https://doi.org/10.1016/J.ADDMA.2020.101514.

[25] A. Bin Anwar, Q.C. Pham, Study of the spatter distribution on the powder bed during selective laser melting, Addit. Manuf. 22 (2018) 86–97, https://doi.org/10.1016/j.addma.2018.04.036.

[26] C.L.A. Leung, S. Marussi, M. Towrie, R.C. Atwood, P.J. Withers, P.D. Lee, The effect of powder oxidation on defect formation in laser additive manufacturing, Acta Mater. 166 (2019) 294–305, https://doi.org/10.1016/j.actamat.2018.12.027.

[27] C. Schwerz, L. Nyborg, A neural network for identification and classification of systematic internal flaws in laser powder bed fusion, CIRP J. Manuf. Sci. Technol. 37 (2022) 312–318, https://doi.org/10.1016/J.CIRPJ.2022.02.010.

[28] C. Schwerz, L. Nyborg, Linking in situ melt pool monitoring to melt pool size distributions and internal flaws in laser powder bed fusion, Met. 2021, Vol. 11, Page 1856 11 (2021) 1856, https://doi.org/10.3390/MET11111856.

[29] T. Lindeberg, Detecting salient blob-like image structures and their scales with a scale-space primal sketch: a method for focus-of-attention, Int. J. Comput. Vis. 11 (1993) 283–318, https://doi.org/10.1007/BF01469346.

[30] H. Kong, H.C. Akakin, S.E. Sarma, A generalized laplacian of gaussian filter for blob detection and its applications, IEEE Trans. Cyber 43 (2013) 1719–1733, https://doi.org/10.1109/TSMCB.2012.2228639.

[31] Y. Xu, T. Wu, F. Gao, J.R. Charlton, K.M. Bennett, Improved small blob detection in 3D images using jointly constrained deep learning and Hessian analysis, Sci. Rep. 2020 101 (10) (2020) 1–12, https://doi.org/10.1038/s41598-019-57223-y.

[32] B.A. Bircher, F. Meli, A. Küng, R. Thalmann, Metrological X-ray computed tomography at sub-micrometre precision, Euspen's 20th Int. Conf. Exhib. (Geneva, Switz.) (2020) 1–4.

[33] B.A. Bircher, F. Meli, A. Küng, R. Thalmann, A geometry measurement system for a dimensional cone-beam CT, 8th Conf. Ind. Comput. Tomogr. Wels, Austria (ICT 2018). (2018) 1–7.

[34] B.A. Bircher, S. Wyss, D. Gage, A. Küng, C. Körner, F. Meli, High-resolution X-ray computed tomography for additive manufacturing: Towards traceable porosity defect measurements using digital twins, Euspen SIG Adv. Precis, Addit. Manuf. (2021) 3–6.

[35] C. Schwerz, F. Schulz, E. Natesan, L. Nyborg, Increasing productivity of laser powder bed fusion manufactured Hastelloy X through modification of process parameters, J. Manuf. Process 78 (2022) 231–241, https://doi.org/10.1016/J.JMAPRO.2022.04.013.

[36] N.T. Aboulkhair, N.M. Everitt, I. Ashcroft, C. Tuck, Reducing porosity in AlSi10Mg parts processed by selective laser melting, Addit. Manuf. 1 (2014) 77–86, https://doi.org/10.1016/j.addma.2014.08.001.

[37] S. Kou. Welding Metallurgy, 2nd ed., John Wiley & Sons, Inc, 2003 https://doi.org/10.1002/0471434027.

[38] P.J. Rousseeuw, Silhouettes: a graphical aid to the interpretation and validation of cluster analysis, J. Comput. Appl. Math. 20 (1987) 53–65, https://doi.org/10.1016/0377-0427(87)90125-7.

[39] R. Snell, S. Tammas-Williams, L. Chechik, A. Lyle, E. Hernández-Nava, C. Boig, G. Panoutsos, I. Todd, Methods for rapid pore classification in metal additive manufacturing, JOM 72 (2020) 101–109, https://doi.org/10.1007/s11837-019-03761-9.

[40] R. Cunningham, S.P. Narra, C. Montgomery, J. Beuth, A.D. Rollett, Synchrotron-based X-ray microtomography characterization of the effect of processing variables on porosity formation in laser power-bed additive manufacturing of Ti-6Al-4V, JOM 69 (2017) 479–484, https://doi.org/10.1007/s11837-016-2234-1.

[41] M. Taheri Andani, R. Dehghani, M.R. Karamooz-Ravari, R. Mirzaeifar, J. Ni, A study on the effect of energy input on spatter particles creation during selective laser melting process, Addit. Manuf. 20 (2018) 33–43, https://doi.org/10.1016/j.addma.2017.12.009.

[42] A.R. Nassar, M.A. Gundermann, E.W. Reutzel, P. Guerrier, M.H. Krane, M.J. Weldon, Formation processes for large ejecta and interactions with melt pool formation in powder bed fusion additive manufacturing, Sci. Rep. 9 (2019) 1–11, https://doi.org/10.1038/s41598-019-41415-7.

[43] C. Schwerz, Y. Cao, L. Nyborg, Surface chemical analysis of spatter particles generated in laser powder bed fusion of Hastelloy X in process atmospheres with high and low oxygen content, Surf. Interface Anal. (2023), https://doi.org/10.1002/SIA.7202.

[44] P.A. Hooper, Melt pool temperature and cooling rates in laser powder bed fusion, Addit. Manuf. 22 (2018) 548–559, https://doi.org/10.1016/J.ADDMA.2018.05.032.

[45] Y. Mahmoodkhani, U. Ali, S. Imani Shahabad, A. Rani Kasinathan, R. Esmaeilizadeh, A. Keshavarzkermani, E. Marzbanrad, E. Toyserkani, On the measurement of effective powder layer thickness in laser powder-bed fusion additive manufacturing of metals, Prog. Addit. Manuf. 4 (2019) 109–116, https://doi.org/10.1007/s40964-018-0064-0.

[46] U. Ali, Y. Mahmoodkhani, S.I. Shahabad, R. Esmaeilizadeh, F. Liravi, E. Sheydaeian, K.Y. Huang, E. Marzbanrad, M. Vlasea, E. Toyserkani, On the measurement of relative powder-bed compaction density in powder-bed additive manufacturing processes, Mater. Des. 155 (2018) 495–501, https://doi.org/10.1016/j.matdes.2018.06.030.

[47] C. Gobert, E. Arrieta, A. Belmontes, R.B. Wicker, F. Medina, B. McWilliams, Conditional generative adversarial networks for in-situ layerwise additive manufacturing data, 2019.

[48] H. Chen, Q. Wei, Y. Zhang, F. Chen, Y. Shi, W. Yan, Powder-spreading mechanisms in powder-bed-based additive manufacturing: Experiments and computational modeling, Acta Mater. 179 (2019) 158–171, https://doi.org/10.1016/J.ACTAMAT.2019.08.030.

[49] H. Chen, Q. Wei, S. Wen, Z. Li, Y. Shi, Flow behavior of powder particles in layering process of selective laser melting: Numerical modeling and experimental verification based on discrete element method, Int. J. Mach. Tools Manuf. 123 (2017) 146–159, https://doi.org/10.1016/J.IJMACHTOOLS.2017.08.004.